LES of turbulent square jet flow using an MRT lattice Boltzmann model

Huidan Yu [a], Li-Shi Luo [b,*], Sharath S. Girimaji [a]

[a] *Aerospace Engineering Department, Texas A&M University, College Station, TX 77840-3141, USA*
[b] *Department of Mathematics and Statistics, Old Dominion University, Norfolk, VA 23529, USA*

Abstract

In this paper we consider the application of multiple-relaxation-time (MRT) lattice Boltzmann equation (LBE) for large-eddy simulation (LES) of turbulent flows. The implementation is discussed in the context of 19-velocity (D3Q19) MRT-LBE model in conjunction with the Smagorinsky subgrid closure model. The MRT-LBE-LES is then tested in the turbulent square jet flow case. We compare MRT-LBE-LES results with (a) single-relaxation-time (SRT) or BGK LBE results and (b) experimental data. Computed results include the distribution of centerline mean streamwise velocity, jet spread, and spanwise profiles of mean streamwise velocity in the near-field region. The phenomenon of axis switching is investigated. The advantages of MRT over SRT are demonstrated. Reasonable agreement between our numerical results and experimental data demonstrate that the MRT-LBE is a potentially viable tool for LES of turbulence.
© 2005 Elsevier Ltd. All rights reserved.

1. Introduction

The lattice Boltzmann equation (LBE) [1,2] is now well established as an accurate and efficient method for direct numerical simulations (DNS) of simple turbulent flows (cf. reviews [3–5] and references therein). However, the efficiency and accuracy of LBE method have not been thoroughly investigated for large eddy simulations (LES) of turbulence. Although LES based on the LBE with Smagorinsky model was proposed early on [6–8], it is only recently the LBE-LES has been applied to some more realistic flows [9–16].

In the literature, the lattice Boltzmann equation with the single-relaxation-time (SRT) approximation or Bhatnagar–Gross–Krook (BGK) [17] model is the most popular scheme [18,19] due to its simplicity. However, the simplicity of the lattice BGK (LBGK) model comes at the expense of numerical instability [20] and inaccuracy in implementing boundary conditions [21,22]. These deficiencies in the

LBGK models can be overcome with the use of multiple-relaxation-time (MRT) model as described in [20,23–25]. It has been clearly demonstrated that the LBE models with MRT collision operators have inherent advantages over their LBGK counterparts [20–25]. The LBE model used in the present work is a three dimensional (3D) 19-velocity (D3Q19) model with MRT collision operator [24]. The implementation of MRT-LBE in the LES context entails a number of important formulations such as the calculation of the strain-rate tensor from the non-equilibrium moments. In the Smagorinsky model, the subgrid stress is determined from the strain-rate tensor. Hence precise determination of strain-rate tensor from non-equilibrium moments is crucial for accurate LES implementation.

The objectives of this paper are to: (a) devise efficient schemes for numerical implementation of MRT-LBE for LES with Smagorinsky subgrid closure model; (b) perform comparative assessment of MRT-LBE and SRT-LBE methods for a challenging test case; and, (c) compare MRT-LBE-LES computations against experimental data for that test case. The turbulent square jet is chosen as the test case for this study as it exhibits many complex features such as axis-switching. Turbulent square jet has been previously studied by means of experiments and

---

* Corresponding author.
E-mail addresses: h0y5840@aero.tamu.edu (H. Yu), lluo@odu.edu, luo@nianet.org (L.-S. Luo), girimaji@aero.tamu.edu (S.S. Girimaji).
URL: http://www.lions.odu.edu/~lluo (L.-S. Luo).

Navier–Stokes based simulations [26,27] and a reasonably complete data set is available for comparison and evaluation. The turbulent square jet considered in this study is of $Re = 184,000$.

The remainder of this paper is organized as follows. Section 2 describes the LES formulation of MRT-LBE with the Smagorinsky subgrid scale model. In Section 3 we compare the MRT and SRT flow fields and assess the differences. In Section 4 we evaluate MRT-LBE-LES results against experimental data. We close with a discussion in Section 5. Appendix A discusses the implementation of the MRT-LBE method and calculation of the strain-rate tensor from nonequilibrium moments.

2. D3Q19 MRT-LBE with Smagorinsky model

For a MRT-LBE model with Q velocities, a set of velocity distribution functions $\{f_\alpha | \alpha = 0, 1, \ldots, Q-1\}$ is defined on each lattice node $\boldsymbol{x}_i$. The collision is executed in the moment space $\mathbb{M} = \mathbb{R}^Q$, while the advection is performed in the velocity space $\mathbb{V} = \mathbb{R}^Q$ [24]. The evolution equation for the MRT-LBE on a D-dimensional lattice $\delta_x \mathbb{Z}_D$ with discrete time $t_n \in \delta_t \mathbb{N}_0$ is

$$\mathbf{f}(\boldsymbol{x}_i + \boldsymbol{e}\delta_t, t_n + \delta_t) - \mathbf{f}(\boldsymbol{x}_i, t_n) = \boldsymbol{\Omega}(\boldsymbol{x}_i, t_n)$$
$$= -\mathsf{M}^{-1} \cdot \hat{\mathsf{S}} \cdot [\mathbf{m} - \mathbf{m}^{(eq)}], \quad (1)$$

where M is a $Q \times Q$ matrix which linearly transforms the distribution functions $\mathbf{f} \in \mathbb{V}$ to the velocity moments $\mathbf{m} \in \mathbb{M}$:

$$\mathbf{m} = \mathsf{M} \cdot \mathbf{f}, \quad \mathbf{f} = \mathsf{M}^{-1} \cdot \mathbf{m}. \quad (2)$$

We use the bold-face symbols to denote column vectors as the following:

$$\mathbf{f}(\boldsymbol{x}_i + \boldsymbol{e}\delta_t, t_n + \delta_t)$$
$$:= (f_0(\boldsymbol{x}_i, t_n + \delta_t), \ldots, f_Q(\boldsymbol{x}_i + \boldsymbol{e}_Q\delta_t, t_n + \delta_t))^\mathsf{T},$$
$$\mathbf{f}(\boldsymbol{x}_i, t_n) := (f_0(\boldsymbol{x}_i, t_n), f_1(\boldsymbol{x}_i, t_n), \ldots, f_Q(\boldsymbol{x}_i, t_n))^\mathsf{T},$$
$$\mathbf{m} := (m_0(\boldsymbol{x}_i, t_n), m_1(\boldsymbol{x}_i, t_n), \ldots, m_Q(\boldsymbol{x}_i, t_n))^\mathsf{T},$$
$$\mathbf{m}^{(eq)} := (m_0^{(eq)}(\boldsymbol{x}_i, t_n), m_1^{(eq)}(\boldsymbol{x}_i, t_n), \ldots, m_Q^{(eq)}(\boldsymbol{x}_i, t_n))^\mathsf{T},$$

where T is the transpose operator.

In the D3Q19 MRT-LBE model [24], the 19 discrete velocities are

$$\boldsymbol{e}_\alpha = \begin{cases} (0,0,0), & \alpha = 0, \\ (\pm 1, 0, 0), (0, \pm 1, 0), (0, 0, \pm 1), & \alpha = 1\text{–}6, \\ (\pm 1, \pm 1, 0), (\pm 1, 0, \pm 1), (0, \pm 1, \pm 1), & \alpha = 7\text{–}18. \end{cases}$$

The 19 moments are arranged in the following order: $m_0 = \delta\rho$ is the density fluctuation, $m_1 = e$ is related to energy, $m_2 = \varepsilon$ is related to energy square, $m_{3,5,7} = j_{x,y,z}$ are components of the momentum $\boldsymbol{j} = (j_x, j_y, j_z) = \rho_0 \boldsymbol{u}$, $m_{4,6,8} = q_{x,y,z}$ are related to components of the heat flux $\boldsymbol{q} = (q_x, q_y, q_z)$, $m_9 = 3p_{xx}$, $m_{11} = p_{ww}$ and $m_{13,14,15} = p_{xy,yz,zx}$ are related to the components of the symmetric and traceless strain-rate tensor, $m_{10} = 3\pi_{xx}$ and $m_{12} = \pi_{ww}$

are fourth order moments, and $m_{16,17,18} = m_{x,y,z}$ are third order moments [24].

The quantity ρ_0 is the mean density in the system, which is usually set to 1. The relaxation matrix $\hat{\mathsf{S}}$ is diagonal in the moment space $\mathbb{M}$:

$$\hat{\mathsf{S}} = \text{diag}(0, s_1, s_2, 0, s_4, 0, s_4, 0, s_4, s_9, s_2, s_9, s_2, s_9, s_9, s_9, s_{16}, s_{16}, s_{16})$$
$$= \text{diag}(0, s_e, s_\varepsilon, 0, s_q, 0, s_q, 0, s_q, s_v, s_\pi, s_v, s_\pi, s_v, s_v, s_v, s_m, s_m, s_m). \quad (3)$$

The equilibria of the moments, $\mathbf{m}^{(eq)}$, are the functions of the conserved moments, which are mass density ρ $(=\rho_0 + \delta\rho)$ and momentum density $\boldsymbol{j}$ for athermal fluids, i.e., $\mathbf{m}^{(eq)}(\boldsymbol{x}_i, t_n) = \mathbf{m}^{(eq)}(\rho(\boldsymbol{x}_i, t_n), \boldsymbol{j}(\boldsymbol{x}_i, t_n))$. For the D3Q19 model, the equilibria for the non-conserved moments are given by [24,25]:

$$m_1^{(eq)} = -11\delta\rho + \frac{19}{\rho_0}\boldsymbol{j}\cdot\boldsymbol{j}, \quad m_2^{(eq)} = \omega_\varepsilon\delta\rho + \frac{\omega_{\varepsilon j}}{\rho_0}\boldsymbol{j}\cdot\boldsymbol{j}, \quad (4a)$$

$$m_{4,6,8}^{(eq)} = -\frac{2}{3}j_{x,y,z}, \quad (4b)$$

$$m_9^{(eq)} = \frac{1}{\rho_0}(3j_x^2 - \boldsymbol{j}\cdot\boldsymbol{j}), \quad m_{11}^{(eq)} = \frac{1}{\rho_0}(j_y^2 - j_z^2), \quad (4c)$$

$$m_{10}^{(eq)} = \omega_{xx}m_9^{(eq)}, \quad m_{12}^{(eq)} = \omega_{xx}m_{11}^{(eq)}, \quad (4d)$$

$$m_{13}^{(eq)} = \frac{1}{\rho_0}j_x j_y, \quad m_{14}^{(eq)} = \frac{1}{\rho_0}j_y j_z, \quad m_{15}^{(eq)} = \frac{1}{\rho_0}j_z j_x, \quad (4e)$$

$$m_{16}^{(eq)} = m_{17}^{(eq)} = m_{18}^{(eq)} = 0. \quad (4f)$$

The parameters in the equilibria are chosen as follows to optimize the linear stability of the model: $\omega_\varepsilon = \omega_{xx} = 0$ and $\omega_{\varepsilon j} = -475/63$ [24]. The density fluctuation $\delta\rho$ instead of the total density ρ is used in m_0, $m_1^{(eq)}$ and $m_2^{(eq)}$ to reduce the numerical effects due to the round-off error [28,24].

The speed of sound in the model is $c_s = 1/\sqrt{3}$ in the lattice units of $\delta_x = \delta_t = 1$. And the viscosity is

$$v = \frac{1}{3}\left(\frac{1}{s_v} - \frac{1}{2}\right)c^2\delta_t, \quad c := \frac{\delta_x}{\delta_t}. \quad (5)$$

For LES, $v = v_0 + v_t$, where v_0 and v_t are the molecular viscosity and turbulent viscosity (or eddy viscosity), respectively. In the Smagorinsky model [29,30], the eddy viscosity v_t is determined from the filtered strain rate tensor $S_{\alpha\beta} = (\partial_\alpha u_\beta + \partial_\beta u_\alpha)/2$, a filter length scale Δ_x and the Smagorinsky constant C_S:

$$v_t = (C_S\Delta_x)^2\bar{S}, \quad \bar{S} := \sqrt{2\mathsf{S}:\mathsf{S}}. \quad (6)$$

In the LBE-LES with a uniform mesh, we set $\Delta_x = \delta_x = 1$ and $C_S = 0.1$ [16]. It should be noted that in the LBE-LES, all the quantities involved, i.e., ρ, $\boldsymbol{u}$ and other moments of $\mathbf{f}$, are filtered quantities. Since we are only concerned with LBE-LES, we do not use different symbols to distinguish filtered quantities from the unfiltered ones. In MRT-LBE model, $S_{\alpha\beta}$ can be computed directly from non-equilibrium moments. The formulation of $S_{\alpha\beta}$ is given in Appendix A.

The no-slip boundary conditions in the LBE is realized by the bounce-back boundary conditions [31,32,22]:

$$f_{\tilde{\alpha}}(\boldsymbol{x}_b, t_n + \delta_t) = \tilde{f}_{\alpha}(\boldsymbol{x}_b, t_n) - 6w_{\alpha}\boldsymbol{j}_b \cdot \boldsymbol{e}_{\alpha}$$

$$= \tilde{f}_{\alpha}(\boldsymbol{x}_b, t_n) - 6w_{\alpha}\rho_b\boldsymbol{u}_b \cdot \boldsymbol{e}_{\alpha}, \qquad (7)$$

where $f_{\tilde{\alpha}}$ is the distribution function corresponding to $\boldsymbol{e}_{\tilde{\alpha}} := -\boldsymbol{e}_{\alpha}$, $\tilde{f}_{\alpha}$ denotes the post-collision value of f_{α}, $w_0 = 1/3$, $w_{1-6} = 1/18$ and $w_{7-18} = 1/36$ correspond to the three speed values 0, 1, and $\sqrt{2}$, respectively; and ρ_b and $\boldsymbol{u}_b$ are respectively the density and velocity at the boundary where the bounce-back collision occurs. In what follows, we assume $\rho_b = \rho_0$.

In our simulations, the values for the relaxation rates other than s_v are chosen as the following: $s_1 = 1.19$, $s_2 = s_{10} = 1.4$, $s_4 = 1.2$ and $s_{16} = 1.98$. These values of s_{α} are obtained by optimizing the linear stability of the model [24].

3. Test case and SRT–MRT comparison study

The test case chosen for the present study is turbulent square jet which exhibits unique features such as axis-switching. In this Section, we perform a qualitative comparison of the MRT and SRT flow fields. Validation against experimental data will be performed in the next section.

The coordinate system of the simulation is as follows. The x, y and z axes are the streamwise, spanwise, and lateral directions, as depicted in Fig. 1. The jet exit slot is situated at the center of plane $x = 0$. In this study, we use a uniform mesh of $N_x \times N_y \times N_z = 200 \times 100^2$ for the jet chamber, with the jet exit slot area of $h^2 = 20^2$. The equivalent diameter D_e ($D_e := 2h/\sqrt{\pi}$) of the jet exit is about 22.57. Periodic boundary conditions are applied in both y and z directions. It is found the periodic boundary conditions and fluid at rest boundary conditions yield very similar results [33]. It is demonstrated in [33] that the assumption of periodicity does not affect the jet structure or statistics in the near-field under the given conditions. We impose a uniform velocity and density (pressure) profile for the jet at the exit: $u_0 = 0.1$ and $\rho_0 = 1.0$. The no-slip boundary conditions are applied at the wall with the jet exit slot, located at the upstream end of the jet chamber, and fully-developed flow boundary conditions are applied at the downstream exit of the jet chamber. The molecular

viscosity v_0 is set so that the desired Reynolds number (184,000), is achieved with $u_0 = 0.1$ and $h = 20$ in lattice units. Initially, the system is set at a quiescent state with $\rho = \rho_0 = 1.0$ and $\boldsymbol{u} = \boldsymbol{0}$ except at the jet exit area where $\boldsymbol{u} = u_0\hat{\boldsymbol{x}}$.

The fully-developed boundary conditions are used at the computational outflow boundary:

$$\mathbf{f}(N_x, t_n) = \mathbf{f}(N_x - 1, t_n). \qquad (8)$$

This condition enforces vanishing spatial derivatives along streamwise direction (x) on all quantities of interest. The use of fully-developed boundary outflow conditions deserves further explanation. As LES is an inherently unsteady computation, the outflow will certainly be time-dependent and spatially varying. However, it is difficult, if not impossible, to specify time and space dependent outflow conditions in a spatially developing turbulent flow. The use of this unrealistic outflow condition renders the computed solution non-physical in a region immediately preceding the outflow boundary. This region which is influenced by the fully-developed flow conditions is called the buffer zone. The sole purpose of this zone is to insulate the physically accurate computational zone from the fully-developed outflow conditions. It has been found from experience that the length of buffer region should be a few integral length scales of the flow. In the present case, the buffer region accounts for about the last third (1/3) of the entire computational domain.

Starting from the prescribed initial conditions, the results are computed for a long enough time to allow for the establishment of statistically stationary turbulent field. Then instantaneous fields of the MRT and SRT simulations are examined. Fig. 2 shows contours of the instantaneous MRT flow fields (left) vs. the corresponding SRT (LBGK) fields at a mid-field jet cross-section (yz plane). Recall that SRT and MRT simulations are performed with identical initial and boundary conditions. Clearly, the MRT instantaneous flow fields differ significantly from their SRT counterparts. The difference is most evident in the pressure fluctuation field δp. Significant differences are also seen in the spanwise and lateral velocities u_y and u_z. It is very clear that significant small-scale (of the order of grid size) oscillations are present in the SRT flow fields.
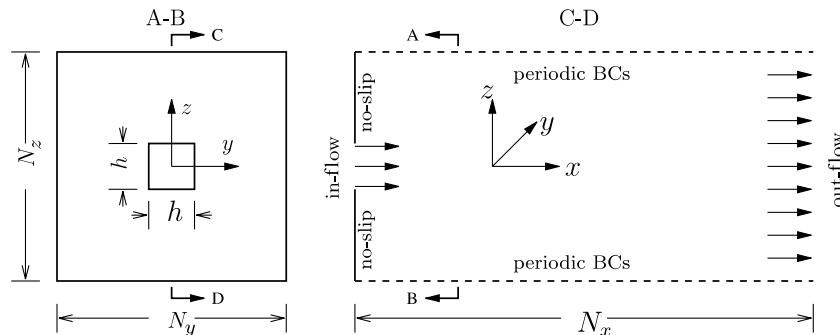

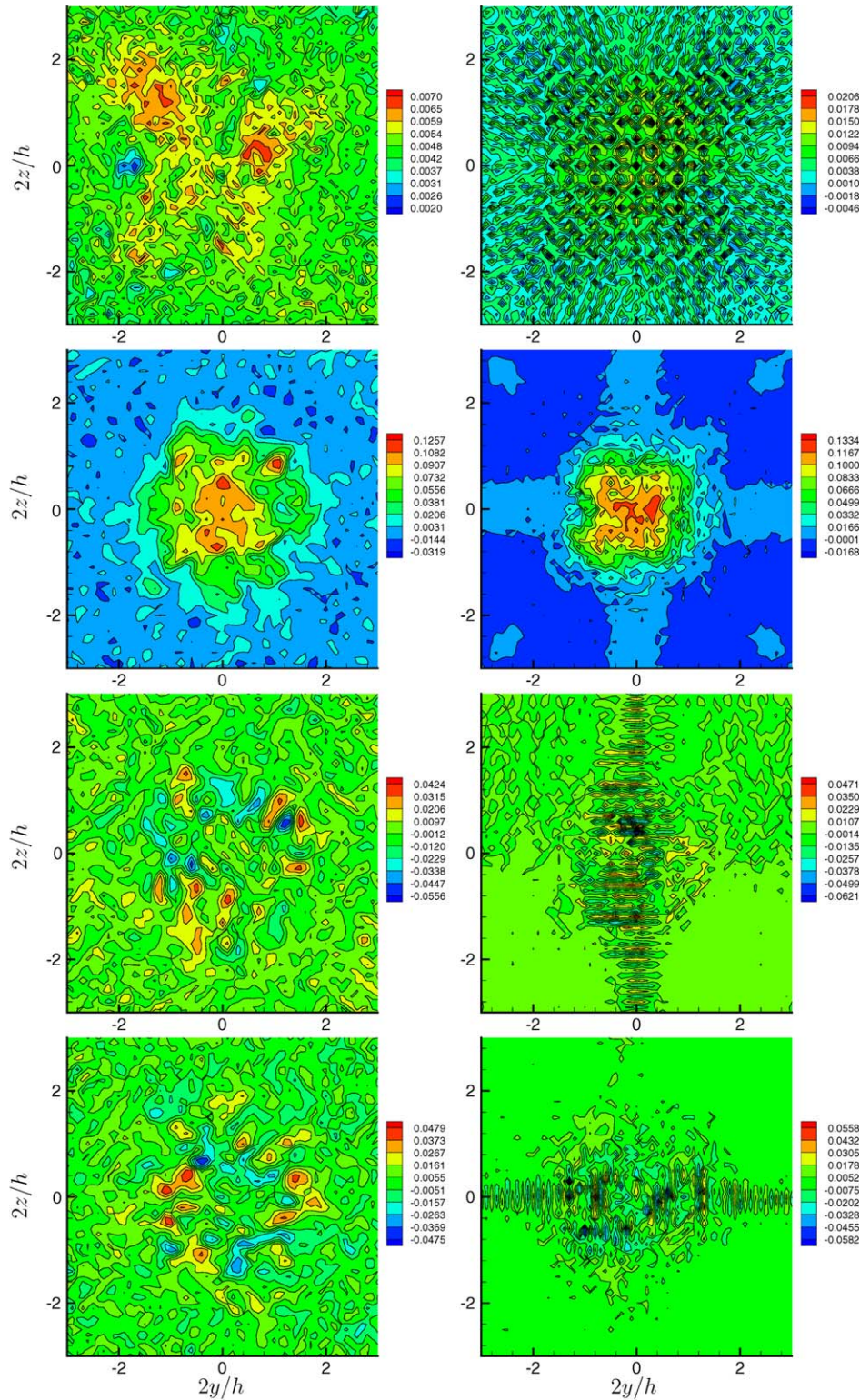Fig. 1. Computational domain and geometry of the jet chamber.

Fig. 2. Contours of instantaneous flow fields on y–z plane, MRT (left) vs. SRT (right). From top to bottom: the pressure fluctuation δp at $x/h = 8$; the streamwise velocity u_x, the spanwise velocity u_y and the lateral velocity u_z at $x/h = 2$.

This computational noise is not evident in the MRT flow fields. We expect that the oscillations seen in the SRT are predominantly due to the spurious conserved quantities in the system [34]. To show that the spurious conserved quantities are indeed responsible for the small-scale oscilla-

tions observed in the SRT flow fields, we average the flow fields over two consecutive time steps and the results are shown in Fig. 3. Clearly, the noise is much reduced in the averaged SRT flow fields. This is especially noticeable for u_y and u_z, as shown in Fig. 3. Similar averaging over two
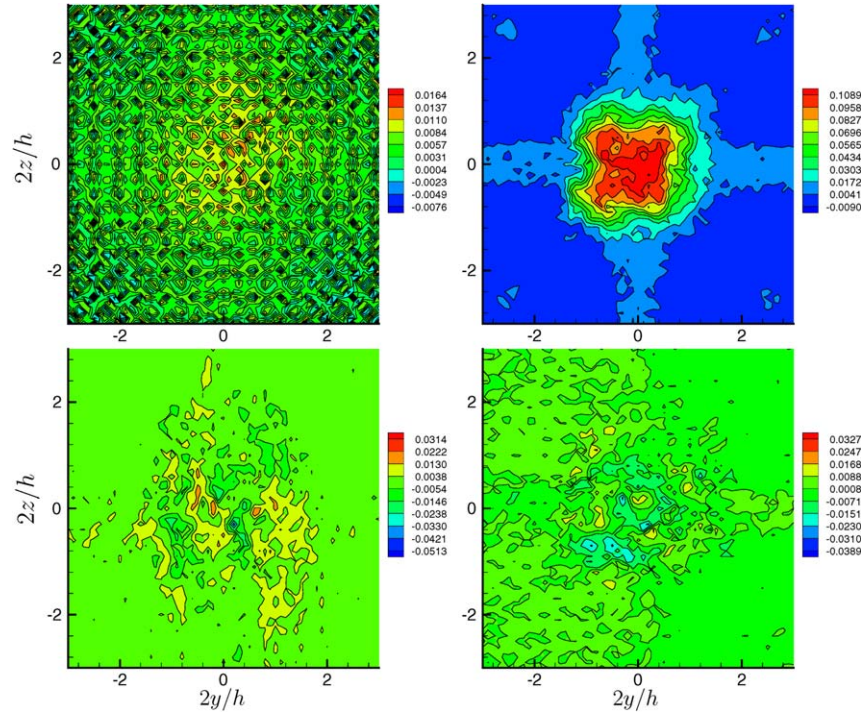
Fig. 3. Contours of flow fields averaged over two consecutive time steps, corresponding to the SRT (LBGK) results in Fig. 2. Clockwise from top-left: the pressure fluctuation δp at $x/h = 8$, the streamwise velocity u_x, the lateral velocity u_z and the spanwise velocity u_y at $x/h = 2$.

consecutive steps of MRT results yields very little change (figure not shown). Thus, the observed SRT oscillation has the symmetry of $(-1)^t$ and checker-board spatial pattern, which is characteristic of the spurious conserved quantities [34]. Even when the oscillation is smoothed out by averaging, there is substantial difference between MRT and SRT results. It will be shown in the next section that MRT results are consistent with experimental data. Evidently, the spurious conserved quantities affect the hydrodynamic variables resulting in a physical degradation of the results. The evidence is most apparent in the averaged SRT pressure figure (top-left of Fig. 3) in which the field is clearly non-physical even after the grid-level oscillations are removed.

The spurious conserved quantities in the LBE are directly coupled to density fluctuations. Depending upon the boundary conditions and number of grid points, the spurious conserved quantities can persist in the computational domain if the dissipation by means of the bulk viscosity is insufficient. There are two easy ways to suppress the oscillations due to the spurious conserved quantities. One is to use appropriate boundary conditions, such as interpolations, to destroy the symmetry of the spurious conserved quantities. The other is to introduce an appropriate amount of the bulk viscosity to dissipate the oscillations. In the MRT-LBE, sufficient bulk viscosity is introduced by design to quickly dissipate any non-physical oscillations due to spurious conserved quantities. It is for this very same reason that MRT models are more stable than their LBGK counterparts. As shown in Fig. 2, the

spurious oscillations degrade the pressure field and ultimately the velocity field in a typical SRT computation.

4. Comparison of MRT-LBE-LES against experimental data

The turbulent square jet has been studied experimentally and numerically [26]. In the experimental study of square jet by Quinn and Militzer [26], the jet is generated in a $76^2 \times 123$ (cm^3) settling chamber with a curved contraction connected to a square jet exit slot of area 4×4 (mm^2), from which the jet issues into a $244^2 \times 366$ (cm^3) chamber. The mean streamwise velocity at the center of the slot exit u_0 is 60 (m/s). The Reynolds number is about 184,000, based on the slot side dimension h (4 (mm)), u_0 and the viscosity of air. We will use this data from the experiment in the validation study. We will restrict ourselves to MRT-LBE-LES in this investigation. In this preliminary study we first seek to establish the viability of MRT-LBE for LES. More detailed comparisons between LES and experimental data for square and rectangular jets will be undertaken in [33].

The computational set-up is exactly same as in the previous case except that the domain size is increased to $N_x \times N_y \times N_z = 500 \times 100^2$ to capture the near-field jet decay. We caution that an exact comparison is not possible as the precise turbulent unsteady inflow data is unavailable. We use a simple laminar top-hat inflow profile. We will restrict our comparison to those quantities which are not sensitive to the exact details of the inflow.

To ensure stationarity of the statistics of time-averaged flow field, we have conducted a series of tests to quantitatively measure the influence of initial run time and the averaging time with a given domain size and for each case computed. With the specific domain size of $N_x \times N_y \times N_z = 500 \times 100^2$, we observe that an initial run time of $25T_0$ ($T_0 := D_e/u_0$) and an averaging time of $35T_0$ are sufficient for the square jet flow, and that a longer initial run time and/or a longer averaging time make negligible difference in the averaged flow field. Thus, the data presented in this section are obtained with an initial run time of $25T_0$ and an averaging time of $35T_0$.

First, we investigate the phenomenon of axis-switching which is unique to non-circular jets. Fig. 4 shows the contours of the mean streamwise velocity $u_x(x, y, z)$ normalized by the mean centerline velocity $u_{cl}(x)$, i.e., $u_x(x, y, z)/u_{cl}(x) = 1/2$, on several cross sections along the streamwise direction (x). These contour lines qualitatively represent the jet shape and our primary interest is the manner in which this shape changes along the downstream direction. Very close to the exit at $x = 0.0625h$, the jet shape is dictated by the jet exit geometry and is clearly a square with sharp corners and its edges parallel to the jet exit slot (solid line in Fig. 4). Further away from the jet exist at $x = 0.5h$, the shape is significantly deformed and becomes more round (dash line in Fig. 4). Finally, further down stream at $x = 2.0h$, the contour shape becomes a square approximately, but with a 45° rotation with respect to the jet exit slot. In other words, the contour shape has "switched" its principle axes by 45° as the jet evolves along streamwise direction. The contour surface of $u_x(x, y, z)/u_{cl}(x) = 1/2$ depicted in Fig. 5 clearly shows the axis-switching. Thus, the LBE-LES simulation captures the same phenomenon
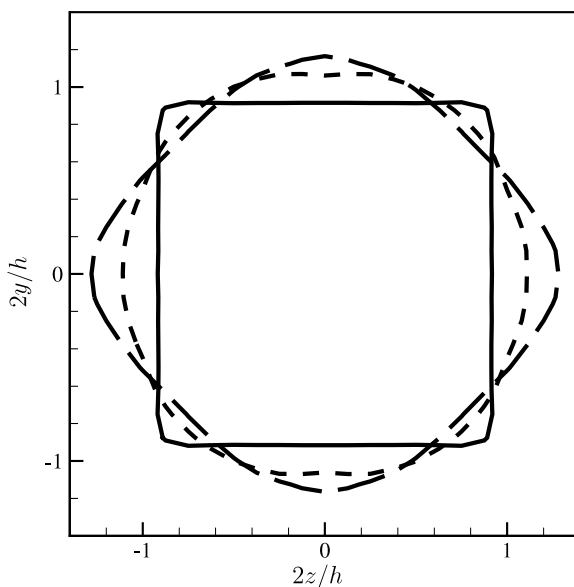

Fig. 5. 3D contour surface of the normalized mean streamwise velocity $u_x(x, y, z)/u_{cl}(x) = 1/2$, $0 \leqslant x \leqslant 5.0h$.

which has been observed previously by experiment and NS-based simulations [27].

In any jet study, three quantities are of primary interest: (a) the extent of jet penetration into the ambient; (b) the degree of jet spread or entrainment and (c) the evolution of the velocity profile of the jet. We now compare the simulation results with experimental data in these three categories.

The extent of penetration is best quantified by the rate of decrease of the centerline velocity u_{cl} of the jet. Slow decrease of the centerline velocity would indicate deeper penetration of the jet into the ambiance. The computed mean streamwise velocity evolution on the jet centerline is shown in Fig. 6 along with the experimental result of Quinn and Militzer [26]. The centerline velocity u_{cl} is normalized with u_{max} which is the maximum mean streamwise velocity along the jet centerline. The maximum centerline velocity u_{max} is not at the jet exit but at *Vena Contracta* located approximately at $x/D_e \approx 1.5$. The *Vena Contracta* effect is more pronounced in the experiment [26] than in the simulations. This is due to the difference in the jet exit velocity profile in the two cases. In the experiment the jet exit profile is not uniform due to the curvature in the

Fig. 4. Contours of the normalized mean streamwise velocity $u_x(x, y, z)/u_{cl}(x) = 1/2$ at different locations along the streamwite direction. Solid, dash and long-dash lines correspond to $x = 0.0625h$, $0.5h$ and $2.0h$, respectively.
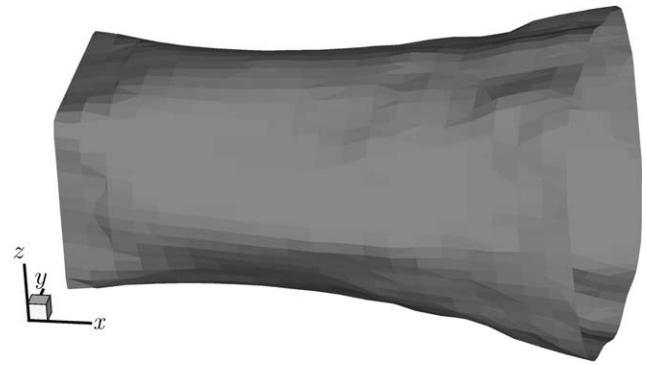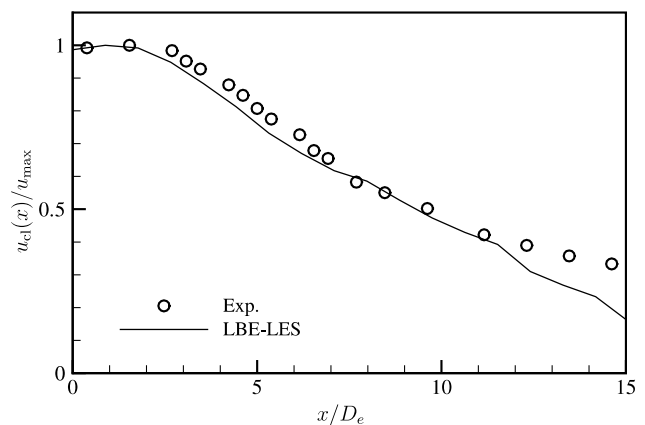

Fig. 6. Decay of the mean centerline streamwise velocity $u_{cl}(x)$ normalized by the maximum velocity u_{max}. The experimental data (○) are taken from Fig. 3 in [26].
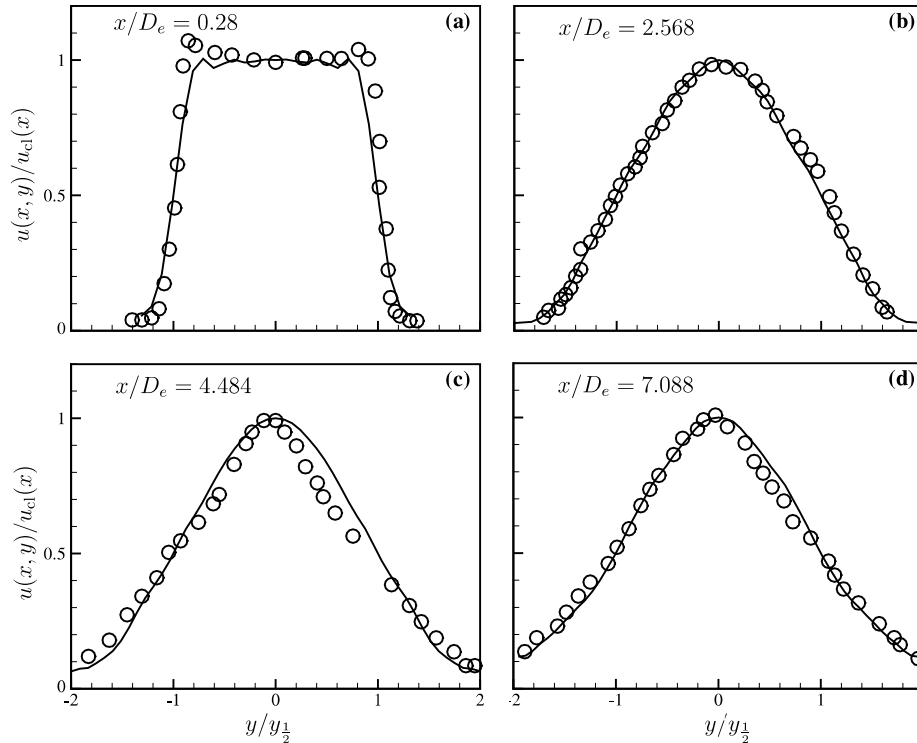
Fig. 7. Mean streamwise velocity profiles in the central xy plane ($z = 0$) at different locations. (a) $x/D_e = 0.28$, (b) $x/D_e = 2.658$, (c) $x/D_e = 4.484$ and (d) $x/D_e = 7.088$. Experimental data ($\bigcirc$) are taken from Fig. 5 in [26].

streamlines as they emerge from the plenum chamber [26]. This profile strongly depends on the plenum chamber geometry and jet-exit details. Thus, the profile can change significantly from one experiment to the other. Here, we do not attempt to address this issue and use a simple plug (uniform) jet-exit velocity profile. We focus on the agreement between the simulations and experiment in the region $2 \leqslant x/D_e \leqslant 15$. The results show that beyond the *Vena Contracta*, the mean streamwise velocity decreases monotonically. Although the *Vena Contracta* effect is not captured precisely, the LBE results agree adequately well with the experimental data in the region of interest. To produce better agreement in the jet exit region $x/D_e < 2$, a better physical description of the plenum chamber and finer grid resolution are required.

Fig. 7 shows the near field spanwise profiles of the mean streamwise velocity on the xy plane at different streamwise locations $x/D_e = 0.28$, 2.688, 4.484 and 7.088. In Fig. 7, the velocity half-width $y_\frac{1}{2}$ of the jet in the spanwise direction is the distance between the jet centerline and the location where the mean streamwise velocity is half that of the centerline. The values of $y_\frac{1}{2}$ are directly measured from velocity profiles shown in Fig. 7. Very good agreement at all locations along streamwise direction between the experimental and LBE-LES results is seen. It is somewhat surprising that the simulations capture the experimental profile in the pre-*Vena Contracta* region (e.g., $x/D_e = 0.28$) reasonably well. However, it should be noted that in these comparisons the streamwise velocity is normalized by the centerline velocity $u_{cl}(x)$, as opposed to the maximum velocity u_{max}.

The next quantity of interest is the jet spread rate. One quantitative measure of the spread rate is the jet half-width $y_\frac{1}{2}$. Clearly, this will be a strong function of downstream location. Rapid increase of the jet half-width with downstream distance would indicate rapid mixing or spreading. The computed variation of the half-width with downstream distance along jet centerline is shown in Fig. 8. Also shown in the figure for comparison are the experimental data and Reynolds-averaged Navier–Stokes numerical data (k–ε model) of Quinn and Militzer [26]. Again, the agreement between experimental data and numerical data from LBE simulation and Navier–Stokes computation is adequate except the very near region ($x/D_e < 4$). In this region, the experiment exhibits a spread-contract-spread behavior which is not well captured by either LBE or RANS calculations. It is not clear whether the observed experimental behavior is due to the *Vena Contracta* effect or a simpler consequence of the jet exit slot geometry. In either case, accurate simulation of this feature again requires a better representation of the plenum chamber flow including the details of jet exit geometry.

We do not present any results of turbulent quantities such as turbulence intensities and shear stresses, as they—unlike the mean quantities—are strongly influenced by inflow unsteadiness and boundary conditions. We do not include the intermediate/far-field in our current simulations due to exorbitant computational costs such a simulation will incur. In this preliminary investigation, many factors that can significantly improve the agreement between simulations and the experiment have not been
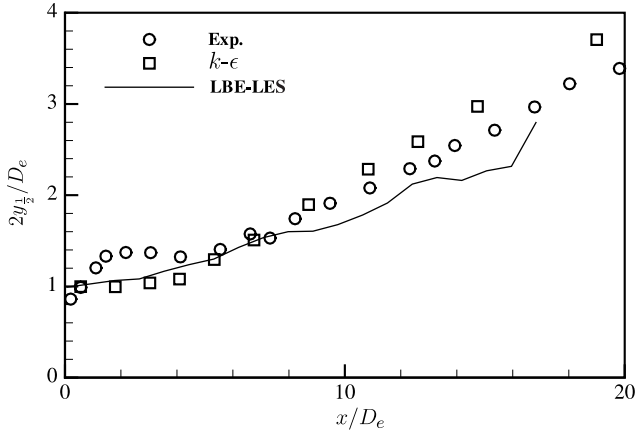
Fig. 8. Development of the jet half-width $y_{\frac{1}{2}}$ along the jet centerline. Experimental ($\bigcirc$) and Navier–Stokes ($\square$) data are taken from Fig. 6 in [26].

optimized. Further studies of turbulent jets of different configurations that represent the experiments more accurately are currently underway [33].

5. Conclusions

In this work, we devise an efficient strategy for implementing the D3Q19 MRT-LBE model with the Smagorinsky sub-grid closure for large eddy simulation of turbulent flows. Numerical evaluation of MRT-LBE-LES is performed in a 3D turbulent square jet flow at $Re = 184{,}000$. A comparative study of MRT and SRT methods shows that the latter model is prone to numerical oscillations that can degrade the quality of the results. In the MRT-LBE-LES, such oscillations are preempted by suitably specifying the bulk viscosity. The MRT LBE-LES results are next compared with experimental data for the following quantities: the mean streamwise velocity, the spanwise profiles of mean streamwise velocity at different down-stream locations and the jet spread. Simulation results are in reasonable agreement with available data. This investigation demonstrates that MRT-LBE is potentially a viable method for LES of turbulent jet flows.

Acknowledgements

Appendix A. Implementation of MRT-LBE for LBE-LES[1]

In this Appendix we wish to address some issues concerning the application of the MRT-LBE models to large-eddy simulations (LES). In implementing the MRT-LBE, it is crucial to understand and utilize the orthogonal property of the transform matrix M so that the programming can be simplified and optimized for numerical efficiency.

The transform matrix M is so constructed that the row vectors $\{\boldsymbol{\varphi}_\alpha^\dagger\}$ are orthogonal to each other, i.e., $\boldsymbol{\varphi}_\alpha^\dagger \cdot \boldsymbol{\varphi}_\beta = \|\boldsymbol{\varphi}_\alpha\|^2 \delta_{\alpha\beta}$ thus $M \cdot M^T$ is a diagonal matrix Φ with diagonal elements $\|\boldsymbol{\varphi}_\alpha\|^2$. Because $M \cdot M^T \cdot \Phi^{-1} = I$, therefore M^{-1} in the collision term of Eq. (1) can be replaced by $M^T \cdot \Phi^{-1}$. The MRT collision term in Eq. (1) can be rewritten as

$$\boldsymbol{\Omega} = -M^T \cdot \Lambda \cdot \mathbf{m}^{(\text{neq})}, \tag{A.1}$$

where $\mathbf{m}^{(\text{neq})} := \mathbf{m} - \mathbf{m}^{(\text{eq})}$ and $\Lambda := \Phi^{-1} \cdot \hat{S}$ is a diagonal matrix with diagonal elements $s_\alpha \|\boldsymbol{\varphi}_\alpha\|^{-2}$. In effect, the relaxation rates $\{s_\alpha\}$ are rescaled to $\{s_\alpha \|\boldsymbol{\varphi}_\alpha\|^{-2}\}$ to account for the normalization of the transformation matrix M.

Thus, with M given, the main steps in the MRT-LBE simulations can be summarized as the following:

- Compute moments $\{m_i\}$ from distribution functions $\{f_i\}$;
- Compute the equilibria $\{m_i^{(\text{eq})}\}$ in the moment space;
- Compute collision term $\boldsymbol{\Omega}$ according to Eq. (A.1) and $\tilde{\mathbf{f}} = \mathbf{f} + \boldsymbol{\Omega}$;
- Advect $\tilde{\mathbf{f}}$ in the velocity space.

Careful coding by hand can reduce repeated calculations thus enhancing computational efficiency [24]. This can be done easily because all the elements in M are integers. For the D3Q19 model, the transformation matrix is

$$
M = \begin{pmatrix}
1 & 1 & 1 & 1 & 1 & 1 & 1 & 1 & 1 & 1 & 1 & 1 & 1 & 1 & 1 & 1 & 1 & 1 & 1 \\
-30 & -11 & -11 & -11 & -11 & -11 & -11 & 8 & 8 & 8 & 8 & 8 & 8 & 8 & 8 & 8 & 8 & 8 & 8 \\
12 & -4 & -4 & -4 & -4 & -4 & -4 & 1 & 1 & 1 & 1 & 1 & 1 & 1 & 1 & 1 & 1 & 1 & 1 \\
0 & 1 & -1 & 0 & 0 & 0 & 0 & 1 & -1 & 1 & -1 & 1 & -1 & 1 & -1 & 0 & 0 & 0 & 0 \\
0 & -4 & 4 & 0 & 0 & 0 & 0 & 1 & -1 & 1 & -1 & 1 & -1 & 1 & -1 & 0 & 0 & 0 & 0 \\
0 & 0 & 0 & 1 & -1 & 0 & 0 & 1 & 1 & -1 & -1 & 0 & 0 & 0 & 0 & 1 & -1 & 1 & -1 \\
0 & 0 & 0 & -4 & 4 & 0 & 0 & 1 & 1 & -1 & -1 & 0 & 0 & 0 & 0 & 1 & -1 & 1 & -1 \\
0 & 0 & 0 & 0 & 0 & 1 & -1 & 0 & 0 & 0 & 0 & 1 & 1 & -1 & -1 & 1 & 1 & -1 & -1 \\
0 & 0 & 0 & 0 & 0 & -4 & 4 & 0 & 0 & 0 & 0 & 1 & 1 & -1 & -1 & 1 & 1 & -1 & -1 \\
0 & 2 & 2 & -1 & -1 & -1 & -1 & 1 & 1 & 1 & 1 & 1 & 1 & 1 & 1 & -2 & -2 & -2 & -2 \\
0 & -4 & -4 & 2 & 2 & 2 & 2 & 1 & 1 & 1 & 1 & 1 & 1 & 1 & 1 & -2 & -2 & -2 & -2 \\
0 & 0 & 0 & 1 & 1 & -1 & -1 & 1 & 1 & 1 & 1 & -1 & -1 & -1 & -1 & 0 & 0 & 0 & 0 \\
0 & 0 & 0 & -2 & -2 & 2 & 2 & 1 & 1 & 1 & 1 & -1 & -1 & -1 & -1 & 0 & 0 & 0 & 0 \\
0 & 0 & 0 & 0 & 0 & 0 & 0 & 1 & -1 & -1 & 1 & 0 & 0 & 0 & 0 & 0 & 0 & 0 & 0 \\
0 & 0 & 0 & 0 & 0 & 0 & 0 & 0 & 0 & 0 & 0 & 1 & -1 & -1 & 1 & 0 & 0 & 0 & 0 \\
0 & 0 & 0 & 0 & 0 & 0 & 0 & 0 & 0 & 0 & 0 & 0 & 0 & 0 & 0 & 1 & -1 & -1 & 1 \\
0 & 0 & 0 & 0 & 0 & 0 & 0 & 1 & -1 & 1 & -1 & -1 & 1 & -1 & 1 & 0 & 0 & 0 & 0 \\
0 & 0 & 0 & 0 & 0 & 0 & 0 & -1 & -1 & 1 & 1 & 0 & 0 & 0 & 0 & 1 & -1 & 1 & -1 \\
0 & 0 & 0 & 0 & 0 & 0 & 0 & 0 & 0 & 0 & 0 & 1 & 1 & -1 & -1 & -1 & -1 & 1 & 1
\end{pmatrix}
. \tag{A.2}
$$

For the LBE-LES, the strain-rate tensor can be computed from the non-equilibrium moments. By approximating the left-hand side of Eq. (1) by its lowest order Taylor expansion in δ_t, we have

$$\mathbf{m}^{(1)} = -\delta_t \hat{S}^{-1} \cdot M \cdot D_t \cdot M^{-1} \cdot \mathbf{m}^{(\text{eq})}, \tag{A.3}$$

where $D_t := \text{diag}(\partial_t, \partial_t + \boldsymbol{e}_1 \cdot \boldsymbol{\nabla}, \ldots, \partial_t + \boldsymbol{e}_{18} \cdot \boldsymbol{\nabla})$, and the term $D_t \mathbf{m}^{(\text{neq})}$ is neglected according to the Chapman–Enskog analysis. Consequently, we have:

$$m_1^{(1)} \approx \frac{38\delta_t}{3s_1}\boldsymbol{\nabla}\cdot\boldsymbol{j}, \quad m_2^{(1)} \approx \frac{(3\omega_\varepsilon+2)\delta_t}{3s_2}\boldsymbol{\nabla}\cdot\boldsymbol{j}, \tag{A.4}$$

$$\boldsymbol{q}^{(1)} := (m_4^{(1)}, m_6^{(1)}, m_8^{(1)}) \approx \frac{42\delta_t}{63s_4}\partial\boldsymbol{j} + \frac{2(22-5\omega_\varepsilon)\delta_t}{63s_4}\boldsymbol{\nabla}\rho, \tag{A.5}$$

$$m_9^{(1)} \approx -\frac{2\delta_t}{3s_9}(3\partial_x j_x - \boldsymbol{\nabla}\cdot\boldsymbol{j}), \quad m_{10}^{(1)} \approx -\frac{\delta_t}{3s_{10}}(3\partial_x j_x - \boldsymbol{\nabla}\cdot\boldsymbol{j}), \tag{A.6}$$

$$m_{11}^{(1)} \approx -\frac{2\delta_t}{3s_9}\left(\partial_y j_y - 2\partial_z j_z\right), \quad m_{12}^{(1)} \approx -\frac{\delta_t}{3s_{10}}\left(\partial_y j_y - 2\partial_z j_z\right), \tag{A.7}$$

$$m_{13}^{(1)} \approx -\frac{\delta_t}{3s_9}\left(\partial_x j_y + \partial_y j_x\right), \quad m_{14}^{(1)} \approx -\frac{\delta_t}{3s_9}\left(\partial_y j_z + \partial_z j_y\right),$$

$$m_{15}^{(1)} \approx -\frac{\delta_t}{3s_9}(\partial_z j_x + \partial_x j_z). \tag{A.8}$$

Therefore, $m_1^{(1)}$, $m_9^{(1)}$ and $m_{11}^{(1)}$ yield the diagonal elements of the strain-rate tensor, while $m_{13}^{(1)}$, $m_{14}^{(1)}$ and $m_{15}^{(1)}$ yield the off-diagonal ones:

$$S_{xx} \approx -\frac{1}{38\rho_0\delta_t}\left(s_1 m_1^{(1)} + 19s_9 m_9^{(1)}\right), \tag{A.9}$$

$$S_{yy,zz} \approx -\frac{1}{76\rho_0\delta_t}\left[2s_1 m_1^{(1)} - 19s_9\left(m_9^{(1)} \mp 3m_{11}^{(1)}\right)\right], \tag{A.10}$$

$$S_{xy,yz,zx} \approx -\frac{3s_9}{2\rho_0\delta_t}m_{13,14,15}^{(1)}. \tag{A.11}$$

We note that while the off-diagonal elements of S are identical to those obtained from the LBGK counterpart, the diagonal elements are not. Because in the MRT calculation, $\boldsymbol{\nabla}\cdot\boldsymbol{j}$ is accounted for, whereas in the LBGK, it is often assumed that $\boldsymbol{\nabla}\cdot\boldsymbol{j} = 0$ and thus the terms related to $\boldsymbol{\nabla}\cdot\boldsymbol{j}$ are ignored.

References

[1] McNamara GR, Zanetti G. Use of the lattice Boltzmann to simulate lattice-gas automata. Phys Rev Lett 1988;61:2332–5.

[2] Higuera FJ, Jimenez J. Boltzmann approach to lattice gas simulations. Europhys Lett 1989;9:663–8.

[3] Chen S, Doolen GD. Lattice Boltzmann method for fluid flows. Annu Rev Fluid Mech 1998;30:329–64.

[4] Luo L-S. The lattice-gas and lattice Boltzmann methods: past, present and future. In: Wu J-H, Zhu Z-J, editors. Proc int conf applied CFD, October 17–20, 2000, Beijing. p. 52–83. Available from http://www.lions.odu.edu/lluo/.

[5] Yu D, Mei R, Luo L-S, Shyy W. Viscous flow computations with the method of lattice Boltzmann equation. Prog Aerospace Sci 2003;39:329–67.

[6] Somers JA. Direct simulation of fluid flow with cellular automata and the lattice-Boltzmann equation. Appl Sci Res 1993;51:127–33.

[7] Eggels JGM. Direct and large-eddy simulation of turbulent flow using the lattice-Boltzmann scheme. Int J Heat Fluid Flow 1996;17:307–23.

[8] Hou S, Sterling J, Chen S, Doolen GD. A lattice Boltzmann subgrid model for high Reynolds number flows. In: Lawniczak AT, Kapral R, editors. Pattern formation and lattice gas automata. Fields Inst Commu, vol. 6, 1996. p. 151–66.

[9] Derksen JJ, Van den Akker HEA. Large eddy simulations on the flow driven by a Rushton turbine. AIChE J 1999;45:209–21.

[10] Derksen JJ, Van den Akker HEA. Simulation of vortex core precession in a reverse-flow cyclone. AIChE J 2000;46:1317–31.

[11] M. Krafczyk, Gitter-Boltzmann-Methoden: Von der Theorie zur Anwendung, Habilitation thesis, Tech Univ Munich 2001.

[12] Lu Z, Liao Y, Qian D, McLaughlin JB, Derksen JJ, Kontomaris K. Large eddy simulations of a stirred tank using the lattice Boltzmann method on a nonuniform grid. J Comput Phys 2002;181:675–704.

[13] Krafczyk M, Tölke J, Luo L-S. Large-eddy simulations with a multiple-relaxation-time LBE model. Int J Mod Phys B 2003;17:33–9.

[14] Hartmann H, Derksen JJ, Montavon C, Pearson J, Hamill IS, Van den Akker HEA. Assessment of large eddy and RANS stirred tank simulations by means of LDA. Chem Eng Sci 2004;59:2419–32.

[15] Yu H, Girimaji S, Luo L-S. Lattice Boltzmann simulations of decaying homogeneous isotropic turbulence. Phys Rev E 2005;71(1):016708.

[16] Yu H, Girimaji S, Luo L-S. DNS and LES of decaying isotropic turbulence with and without frame rotation using lattice Boltzmann method. J Comput Phys 2005;209(2):599–616.

[17] Bhatnagar PL, Gross EP, Krook M. A model for collision processes in gases. I. Small amplitude processes in charged and neutral one-component systems. Phys Rev 1954;94:511–25.

[18] Chen H, Chen S, Matthaeus HW. Recovery of the Navier–Stokes equations using a lattice-gas Boltzmann method. Phys Rev A 1992;45:R5339–42.

[19] Qian Y, d'Humières D, Lallemand P. Lattice BGK models for Navier–Stokes equation. Europhys Lett 1992;17:479–84.

[20] Lallemand P, Luo L-S. Theory of the lattice Boltzmann method: Dispersion, dissipation, isotropy, Galilean invariance, and stability. Phys Rev E 2000;61:6546–62.

[21] Ginzburg I, d'Humières D. Multireflection boundary conditions for lattice Boltzmann models. Phys Rev E 2003;68:066614.

[22] Pan C, Luo L-S, Miller CT. An evaluation of lattice Boltzmann schemes for porous medium flow simulation. Comput Fluids, this issue, doi:10.1016/j.compfluid.2005.03.008.

[23] d'Humières D. Generalized lattice-Boltzmann equations. In: Shizgal BD, Weave DP, editors. Rarefied gas dynamics: theory and simulations. Prog astronaut aeronaut, vol. 159, 1992. p. 450–8.

[24] d'Humières D, Ginzburg I, Krafczyk M, Lallemand P, Luo L-S. Multiple-relaxation-time lattice Boltzmann models in three-dimensions. Philos Trans R Soc London A 2002;360:437–51.

[25] Lallemand P, Luo L-S. Theory of the lattice Boltzmann method: acoustic and thermal properties in two and three dimensions. Phys Rev E 2003;68:036706.

[26] Quinn WR, Militzer J. Experimental and numerical study of a turbulent free square jet. Phys Fluids 1988;31:1017–25.

[27] Grinstein FF. Near field dynamics of subsonic free square jets. A computational and experiment study. Phys Fluids 1995;7(6):1483–97.

[28] Skordos PA. Initial and boundary conditions for the lattice Boltzmann method. Phys Rev E 1993;48:4823–42.

[29] Pope SB. Turbulent flows. Cambridge: Cambridge University Press; 2000.

[30] Smagorinsky J. General circulation experiments with the primitive equations: I. The basic equations. Mon Weather Rev 1963;91:99–164.

[31] Luo L-S. Theory of the lattice Boltzmann method: lattice Boltzmann models for nonideal gases. Phys Rev E 2000;62:4982–96.

[32] Bouzidi M, Firdaouss M, Lallemand P. Momentum transfer of a Boltzmann-lattice fluid with boundaries. Phys Fluids 2001;13(11):3452–9.

[33] Yu H, Girimaji S. Near-field turbulent mixing simulations of rectangular jets using lattice Boltzmann method. Phys Fluids 2005;17, in press.

[34] Zanetti G. Hydrodynamics of lattice-gas automata. Phys Rev A 1989;40:1539–48.